Strong-field phenomena caused by ultrashort laser pulses: Effective one- and two-dimensional quantum-mechanical descriptions

A. A. Silaev, M. Yu. Ryabikin, and N. V. Vvedenskii*
Institute of Applied Physics, Russian Academy of Sciences, Nizhny Novgorod 603950, Russia
(Received 5 March 2010; published 16 September 2010)

In this article, we address two strong-field phenomena which attract much attention and can be observed under similar experimental conditions, namely when a gas is ionized by ultrashort laser pulses. The first phenomenon is the excitation of high-order harmonics of the driving field frequency in the electron current, which leads to the generation of extreme UV and soft-x-ray radiation. The second phenomenon is the excitation of a quasi-dc residual current in the laser-produced plasma, which results in the generation of radiation having a frequency below the laser one, e.g., THz waves. We present alternative one- and two-dimensional quantum-mechanical models for the description of such phenomena for the gas consisting of H atoms and the generalization of these models to the various noble gases. The shape of the electrostatic potential produced by an atomic ion is shown to influence significantly the rates of the processes in the dynamics of atomic electron and, even more, the rate of tunneling ionization, which is of utmost importance for the considered phenomena. The results of solving the time-dependent Schrödinger equation with the proposed model potentials are compared with the results of the *ab initio* three-dimensional calculations for the H atom. We find that in a wide range of laser pulse parameters the results obtained with proposed models have much better accuracy than the results provided by the models used earlier.

DOI: 10.1103/PhysRevA.82.033416 PACS number(s): 32.80.Rm, 42.65.Ky, 42.65.Re, 52.50.Jm

I. INTRODUCTION

An important problem in the description of the interaction of strong laser fields with the ionizable medium is calculation of the electron currents excited in the process of this interaction. It is important, e.g., for the description of high-order harmonic generation (HHG) [1–3], which is well-known as a very useful tool for the generation of coherent radiation in the vacuum UV and soft-x-ray wavelength ranges, as well as for the attosecond pulse production [4,5]. The calculation of the electron currents is important also for the description of another phenomenon intensively studied now, namely the generation of coherent terahertz (THz) waves triggered by ionization of the gas by few-cycle laser pulses [6–14].

For the HHG process, one usually calculates the high-frequency spectrum of the dipole acceleration [15], which is proportional to the time derivative of the electron current density. The main physical mechanism leading to the appearance of high frequencies in the dipole acceleration spectrum is the recombination of photoelectrons during their recollisions with the parent ions [16]. This spectrum has a wide plateau ending with a pronounced cutoff in the frequency region, which usually corresponds to the extreme UV or soft-x-ray radiation. In the case of few-cycle laser pulses, in which the field amplitude differs considerably between the adjacent half-periods, spectral selection of the highest harmonics, which are phase-synchronized, allows one to generate single attosecond pulses [17,18]. For the implementation of this generation, stabilization of the carrier-envelope phase (CEP) of few-cycle laser pulses is of the great importance [19].

For the case of the generation of waves having a frequency much lower than the laser one, e.g., THz waves, the key point in the theoretical description is to find the residual current density (RCD) of free electrons, which is proportional to the zeroth harmonic in the Fourier spectrum of the dipole acceleration. This RCD is the initial impact for the polarization of the laser-produced plasma and the excitation of emitting oscillations in it [7–14]. In the general case, the frequencies of these oscillations are determined by the gas pressure and the density of the generated plasma. For a wide range of gas pressure and plasma density, the frequencies of the waves emitted by the plasma lie in the THz frequency band. The recent studies based on both semiclassical [7–14] and *ab initio* quantum-mechanical [12,13] calculations have shown that RCD is strongly dependent on CEP of few-cycle laser pulses, which can be used to monitor CEP by detecting low-frequency (THz) waves. For other laser pulse parameters fixed, there is an optimal CEP, at which the value of RCD is maximum. In case of the optimal CEP, RCD increases exponentially as the duration of the laser pulse decreases, which can yield very high values of the optical-to-THz conversion efficiency [7,12,13].

One of the main approaches to studying the above-mentioned and other strong-field phenomena is based on solving numerically the time-dependent Schrödinger equation (TDSE) for the electron wave function. In early articles dealing with the numerical TDSE solution, usually reduced-dimensionality problems were considered, in which the Coulomb interaction between charged particles is described by means of one-dimensional (1D) or two-dimensional (2D) model potentials. Wider popularity has been gained by the 1D model potential proposed by Javanainen *et al.* [20] for numerical calculations of energy spectra of photoelectrons when studying above-threshold ionization (ATI) of atoms. Far from the charged particle, with which the electron interacts, this potential is asymptotically close to the exact Coulomb potential. At the point where the charged particle is located, neither the potential nor its derivatives have discontinuities or become infinite, therefore this potential was called the "soft-core" potential. Later, Rae *et al.* [21] suggested to refine this

*vved@appl.sci-nnov.ru

potential according to the requirement that the particle binding energy is equal to the experimentally measured value. One-dimensional soft-core potentials were used to simulate various strong-field phenomena including HHG [21,22], generation of attosecond pulses [23,24], atom stabilization [25,26], and enhanced ionization of diatomic molecules [27–29]. Later the 2D analog of the soft-core potential was proposed [30,31]. The use of the 2D soft-core potential allowed one to perform extensive studies in different basically multidimensional problems, for instance, to perform the description of strong-field phenomena in arbitrarily polarized laser fields [30–32] or beyond the dipole approximation [24,33–35].

Due to the rapid advance in the computer capabilities, growing amount of publications presents the description of strong-field phenomena based on numerical solutions of three-dimensional (3D) TDSE in the single-active electron (SAE) approximation. There are also examples of solving the exact TDSE for the two-electron systems such as the He atom [36]. However, the use of the 1D and 2D models has not lost its significance and is still the only one real toolkit to solve many physical problems. Model soft-core potentials are used now to consider the problems which require solving the TDSE repeatedly, e.g., those dealing with spatially inhomogeneous fields including the cases of coupled solutions of the TDSE and the Maxwell equations [37]. The range of such problems includes also the cases of systems with a great number of the degrees of freedom. For example, they may be the problems related to the dissociative ionization of molecules [38–41] or to the nonsequential multielectron processes [42–45]. In addition, low-dimensional effective potentials are used in the studies having little to do with conventionally considered strong-field phenomena [46–48].

However, Rae *et al.* [21] demonstrated that the use of the 1D soft-core potential for calculating the high-frequency spectrum of the dipole acceleration (HHG spectrum) could yield spectral intensities differing by several orders of magnitude from those found by exact solution of the 3D TDSE. A similar conclusion was made by Gordon *et al.* [49], who suggested that a different 1D model potential, which has a cusp at the point of ion location, should be used for calculations of the HHG spectra. At this point, the first derivative of the 1D potential has a discontinuity. For this potential, the scaling of the recombination amplitude [49–51] with the kinetic energy of the electron recolliding with the parent ion is the same as for the Coulomb potential. As was shown in Ref. [49] by comparing with the results of the 3D TDSE calculations for the H atom driven by highly intense ($\sim 10^{15}$ W/cm^2) single-cycle laser pulse, the use of this potential gives more accurate HHG spectrum than when the 1D soft-core potential is used. This potential, which could be called "solid-core" because of the singularity, was used in later work for testing the approximate semianalytical [52] methods developed to describe the dynamics of Coulomb single- and multielectron systems in a strong laser field and for testing the description of the atom stabilization phenomenon in one dimension [53].

Note that the soft-core and solid-core potentials had been considered long before they were proposed in Refs. [20,49] for calculations of ionization-induced phenomena in strong laser fields. As early as 1959, in Ref. [54], as well as in later works [55,56], wave functions of the stationary states in the solid-core potential were studied. Later, the solid-core potential was used to describe the Coulomb interaction between charge carriers encapsulated in quasi-1D nanostructures, which are quantum dots and quantum wires (see Refs. [57–59] and references therein). The soft-core potential was used already in 1986 to describe the Coulomb interaction between the electrons in a two-dimensional degenerate electron gas when the fractional quantum Hall effect was studied [60].

In this article, we show that the use of both the solid-core and soft-core potentials to calculate the HHG spectra in the region of laser pulse parameters, which is rather wide and interesting from the viewpoint of practical applications, can lead to significant errors. Specifically, the use of these potentials yields the values of spectral intensities differing near the cutoff from those yielded by the exact 3D TDSE solution by more than an order of magnitude. When applied to the calculations of RCD, the use of the soft-core and solid-core potentials can also lead to serious disagreement with the results of solving the 3D TDSE. More specifically, the calculations employing these potentials result in serious errors in the determination of the CEP optimal for RCD generation, as well as to an overestimation of the RCD value *per se* by more than an order of magnitude at the optimal CEP value. Precise determination of these parameters is of a great importance for the determination of the conditions optimal for the generation of THz waves and for future experiments aimed at determining CEP of few-cycle laser pulses [6–8,12–14]. We explain the above-mentioned errors by analyzing ionization probabilities and electron recombination amplitudes in these potentials, as well as the motion of electrons in the continuum. Here, we propose new 1D and 2D model potentials, which differ from the potentials proposed earlier near the location of a charged particle, with which the electron interacts. One type of these potentials, which we call "pliant-core" ones, is suggested to be used in calculations of the HHG spectra. It is demonstrated for the pliant-core potentials applied to the H atom that the values of spectral intensities in the HHG spectra agree well with the results yielded by the solution of the 3D TDSE in a rather wide range of intensities ($\sim 10^{14}$–10^{15} W/cm^2), durations ($\sim$2–5 cycles at full width at half maximum of intensity), and wavelengths ($\sim$1–2 μm) of the laser pulses. This article also studies the spectral intensities of HHG as functions of the laser pulse wavelength, which is a rather topical problem nowadays [61–67]. Its topicality is due to the recent advance in the development of infrared laser sources that allow one to increase the maximum energy of the generated XUV and soft-x-ray photons considerably [68]. The other type of proposed potentials, which we call "supersolid-core" ones, is suggested to be used for RCD calculations. It is shown that the probability of tunneling and above-barrier ionization from the supersolid-core potentials agrees with the probability of ionization from the Coulomb potential with high accuracy. As a result, the RCD value calculated with the use of the supersolid-core potentials agrees well with the RCD calculated on the base of the 3D TDSE in a wide range of considered intensities and durations of the laser pulses. We also present the parameters of the pliant-core and supersolid-core potentials, at which the absolute values of the ground-state energy coincide with the ionization potentials of noble-gas atoms, which are

conventionally used in experimental investigations of various strong-field phenomena.

The article is organized as follows. In Sec. II, we describe the statement of the problem and the method of finding HHG spectrum and RCD. In Sec. III, new 1D and 2D potentials are presented, which simulate the electrostatic potential of the ion in the atoms of hydrogen and various noble gases. In Sec. IV, we present the results of numerical calculations obtained by using the 1D and 2D models and compare them with the results of the 3D calculations. Section IV A presents the details of the numerical methods used for solving 1D, 2D, and 3D TDSEs. In Sec. IV B, we calculate the HHG spectra, as well as the dependencies of the HHG spectrum integrated over the specified frequency intervals on the intensity and central wavelength of the laser pulse. In Sec. IV C, we present the results of RCD calculations. In Sec. V, to explain the obtained results, we calculate the static-field ionization rates as well as the recombination amplitudes for the 1D and 2D potentials and compare these results with those for the exact 3D Coulomb potential. The numerical results are discussed in Sec. VI. Section VII contains the summary and conclusions of the research.

II. STATEMENT OF THE PROBLEM

Consider an unperturbed atom placed in a linearly polarized laser pulse with the electric field $E(t)$, which is assumed to be a specified function of time t and directed along the z axis. Let the laser pulse has the intensity $I \sim 10^{13}$–10^{15} W/cm^2 and the wavelength $\lambda_L \sim 0.8$–2 μm. For these parameters, the dipole approximation is valid for the description of the laser-atom interaction [69]. The TDSE for the electron wave function ψ in the length gauge is written as follows:

$$i\hbar\frac{\partial\psi(\mathbf{r},t)}{\partial t} = \left[\frac{\hat{\mathbf{p}}^2}{2m} + V(r) - eE(t)z\right]\psi(\mathbf{r},t), \tag{1}$$

where $\hbar$ is the Planck constant, $e = -|e|$ and m are the charge and mass of the electron, respectively, $\hat{\mathbf{p}} = -i\hbar\nabla$ is the momentum operator, r is the distance between the electron and ion, and $V(r)$ is the electrostatic potential of the ion. Within the 1D problem, the distance is $r = |z|$, in the 2D problem, $r = \sqrt{x^2 + z^2}$, and in the 3D one, $r = \sqrt{x^2 + y^2 + z^2}$, where x, y, and z are the Cartesian coordinates. The initial wave function is specified as the normalized to unity ground-state eigenfunction of the Hamiltonian $\hat{H}_0 = \hat{\mathbf{p}}^2/2m + V(r)$.

Under the action of the electric field, the electron wave packet acquires a time-dependent dipole acceleration [15], which is directed along the z axis. The dipole acceleration (understood here as the expectation value of the electron acceleration) can be expressed as [15]:

$$a(t) = \frac{e}{m}E(t) - \frac{1}{m}\langle\psi|\frac{\partial V}{\partial z}|\psi\rangle. \tag{2}$$

The knowledge of the dipole acceleration allows one to calculate local macroscopic parameters of the medium, in particular, the density of the electron current excited in the laser-produced plasma. The z component of the electron current density, which is equal to

$$j(t) = \frac{eN_g}{m}\langle\psi|\hat{p}_z|\psi\rangle, \tag{3}$$

is related to the dipole acceleration via the equation

$$j(t) = eN_g\int_{-\infty}^{t} a(t')\,dt'. \tag{4}$$

Here, N_g is the initial density of neutral atoms and $\hat{p}_z$ is the z component of the momentum operator. Those components of the current density, which are transverse to the direction of the electric field, are zero, since the wave-packet spreading is symmetric relative to the z axis. As mentioned above, the dipole-acceleration spectrum $|a_\omega|^2$ has a plateau at high frequencies, which exceed by far the laser frequency [4,5].

Along with the high-frequency plateau, the dipole-acceleration spectrum has also the low-frequency part. In what follows, we will consider the zeroth harmonic a_0 of the dipole acceleration, since it is proportional to RCD of free electrons, $j_{\mathrm{RCD}} = eN_g a_0$. When calculating RCD, it is necessary to allow for the fact that after the passage of the laser pulse the total current density $j(t)$ includes, along with RCD, the fast-oscillating current density $j_b(t)$ of the electrons staying in the bound states in the atoms [12,13]. For a low degree of ionization, the contribution of the electrons staying in the bound states to the total current density can be significant. The frequencies of oscillations of $j_b(t)$ are determined by the energies of transitions between the most populated bound states. We calculate the current density $j_b(t)$ as follows. The wave function ψ is multiplied by the window function $f(r)$, which decreases smoothly from unity to zero with increasing r on the scale of several Bohr radii $r_B = 5.29 \times 10^{-9}$cm (as shown by numerical calculations, $10r_B$ is sufficient for the account of all the most populated bound states contributing significantly to the current density). The function obtained, $\psi_b(\mathbf{r},t) = f(r)\psi(\mathbf{r},t)$, is dominated by the bound states, since they are localized near the ion, whereas the ionized wave packet went away from the ion to a significant distance after the passage of the laser pulse. The value of the current density $j_b(t)$ is found as

$$j_b(t) = \frac{eN_g}{m}\langle\psi_b|\hat{p}_z|\psi_b\rangle. \tag{5}$$

The value of j_{RCD} is found as the difference between the total and bound-state current densities:

$$j_{\mathrm{RCD}} = j(t) - j_b(t). \tag{6}$$

III. MODEL POTENTIALS

A. 1D model potentials

To simulate the strong-field phenomena by solving the 1D TDSE, one frequently uses the *soft-core* potential [20,21]. At the point of origin, neither the potential nor its derivatives have discontinuities or become infinite. For the H atom, the 1D soft-core potential is [21]

$$V_{1\mathrm{D}}(z) = -\frac{e^2}{\sqrt{z^2 + 2r_B^2}}, \tag{7}$$

where $2r_B^2$ is the parameter of Coulomb singularity smoothing, chosen so that the absolute value of the ground-state energy in the potential coincides with the ionization potential of the atom [21]. Far from the point of origin this potential is

asymptotically close to the exact Coulomb potential. The same conditions are met with the potential presented in Ref. [49], which has a cusp at the point of origin and could be called the *solid-core* potential. For the H atom, the 1D solid-core potential is

$$V_{1D}(z) = -\frac{e^2}{|z| + r_B}. \tag{8}$$

In this work, we propose two new 1D model potentials simulating the electrostatic potential of the H atom ion, as well as the generalization of these potentials to five different noble-gas atoms. We propose to use one of these potentials for the calculations of the HHG spectra. The second potential is proposed for the RCD calculations. We chose these model potentials from the following family of the 1D potentials, which are asymptotically close to the Coulomb potential far from the point of origin:

$$V_{1D}(z) = -\frac{e^2}{\left(|z|^\alpha + \beta r_B^\alpha\right)^{1/\alpha}}. \tag{9}$$

Here, α and β are the parameters which determine the sharpness of the function $V_{1D}(z)$ near the point of origin and smoothing of the Coulomb singularity, respectively. They determine also the value of the ground-state energy in this potential. We calculated the relation between the parameters α and β at which the absolute value of the ground-state energy in potential (9) coincides with the H atom ionization potential, $I_p = 13.6\,\text{eV}$. This relation is shown in Fig. 1(a). The circles in the figure mark the values of α and β corresponding to the 1D soft-core and solid-core potentials as well as to the 1D potentials proposed in this work.

To calculate the HHG spectra, we propose using the potential (9) with $\alpha = 3/2$. This choice is motivated by the following simple considerations. As will be shown below by an example of the H atom, for the laser-pulse intensities $I \sim 5 \times 10^{14}\,\text{W/cm}^2$, at the cutoff region the spectral intensity $|a_\omega|^2$ found by using the soft-core potential (7) turns out to be underestimated compared with its precise value found from the 3D calculations. The use of solid-core potential (8) yields overestimated values of $|a_\omega|^2$ for the same parameters of the laser pulse. It is evident that the potential ensuring a good agreement with the 3D calculations should be something "in between" the soft-core and solid-core potentials. In the class of potentials defined by Eq. (9), it could be the potential for which $\alpha = 3/2$ [see Fig. 1(a)]. In what follows, the potentials of this kind will be called *pliant-core* potentials. For the H atom, the 1D pliant-core potential is

$$V_{1D}(z) = -\frac{e^2}{\left(|z|^{3/2} + 1.45 r_B^{3/2}\right)^{2/3}}. \tag{10}$$

To calculate RCD, we suggest using potential (9) with $\alpha = 1/2$. At the point of origin it is sharper than solid-core potential, because at this point the first derivative becomes infinite. We will refer to this kind of potentials as *supersolid-core* potentials. For the H atom, the 1D supersolid-core potential is:

$$V_{1D}(z) = -\frac{e^2}{\left(|z|^{1/2} + 0.6 r_B^{1/2}\right)^2}. \tag{11}$$

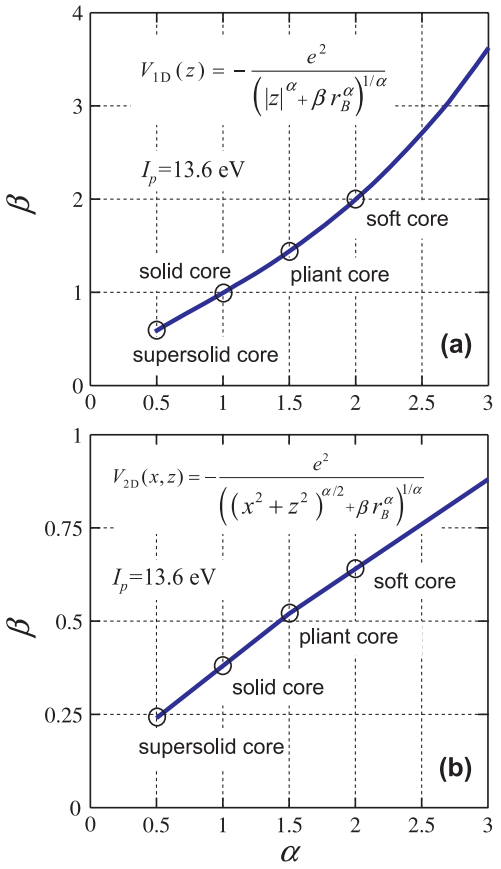

FIG. 1. (Color online) Dependences relating the parameters α and β in the formulas for (a) the 1D and (b) the 2D model potentials [Eqs. (9) and (12)], which were found under the assumption that the absolute value of the ground-state energy in this potential coincides with the hydrogen atom ionization potential. The circles mark the values of the parameters corresponding to the soft-core and solid-core potentials [Eqs. (7), (13) and (8), (16), respectively], as well as the pliant-core and supersolid-core potentials proposed in this work [Eqs. (10), (14) and (11), (15), respectively].

As will be shown below, for this choice of the potential, the probability of tunneling and above-barrier ionization agrees with the ionization probability from the 3D Coulomb potential to a very high accuracy. Therefore, as we will see further, the potentials of this kind are well suited to calculate RCD.

To study the strong-field phenomena in gases consisting of multielectron atoms (such as noble gases), the single-active electron approximation [70] is generally used. Within the SAE approximation, all electrons except one are considered frozen in their orbitals and the field of the parent ion is treated as a simple potential well [70]. The formula for the potential of the parent ion is found from the requirement that the energy of several lowest bound states coincides with the corresponding experimentally measured values [71–73]. We generalize the proposed potentials (10) and (11) to the case of noble-gas atoms. For each species, we fixed the parameter α and calculated the value of the parameter β in order to reach the agreement between the ground-state energy in potential (9) and the experimentally measured value of the ionization potential. Table I presents the results of calculations of the parameter β, rounded to the second significant decimal digit, for $\alpha = 3/2$

TABLE I. Values of the parameter β for the proposed 1D and 2D pliant-core and supersolid-core potentials for hydrogen and noble-gas atoms found under the assumption that the absolute value of the ground-state energy coincides with the atom ionization potential I_p. General expression for the 1D potentials is given by Eq. (9), and for the 2D potentials, by Eq. (12).

		β			
Atom	I_p (eV)	1D pliant core ($\alpha = 1.5$)	1D supersolid core ($\alpha = 0.5$)	2D pliant core ($\alpha = 1.5$)	2D supersolid core ($\alpha = 0.5$)
H	13.60	1.45	0.60	0.52	0.24
He	24.59	0.49	0.38	0.089	0.095
Ne	21.56	0.62	0.42	0.14	0.12
Ar	15.76	1.11	0.54	0.35	0.20
Kr	14.00	1.37	0.58	0.48	0.23
Xe	12.13	1.78	0.65	0.69	0.27

(pliant-core potential) and $\alpha = 1/2$ (supersolid-core potential) for noble gases: He, Ne, Ar, Kr, and Xe. We assume that the use of these model potentials for calculation of the HHG spectra and RCD leads to qualitatively accurate results in the region of parameters of laser pulses, at which the SAE approximation is applicable. This assumption can be checked further by comparing the obtained results with the results of the 3D simulation. There are works where the comparison with the experimental results is used to demonstrate that the 3D simulation within the framework of the SAE approximation allows one to perform qualitatively accurate calculations of the ATI and HHG spectra in the conditions, when the recolliding electrons have moderate kinetic energies, $E_{\rm kin} < 60\,{\rm eV}$ [74,75]. Note that for higher energies of the recolliding photoelectrons in the gases consisting of heavy atoms (e.g., Xe), the HHG process can be strongly influenced by multielectron effects [62], which are not taken into account within the framework of the SAE approximation. Note also that due to the existence of only one degree of freedom of the electron, 1D models are unable to describe the features of the atomic response arising from the details of the atomic valence orbital related to the electron angular momentum. For example, 1D simulations are not expected to describe the Cooper minimum in the HHG spectra [62,75,76] from atoms (Ar, Kr) ionized from p orbitals. On the other hand, the dependence of the continuum electron wave packet on the atomic orbital may be rather weak (see, e.g., Ref. [77]). That is why one can expect sufficiently good performance of proposed reduced-dimensionality models in calculations of RCD for different atoms.

B. 2D model potentials

By analogy with 1D model potentials, we consider the following class of the 2D model potentials:

$$V_{\rm 2D}(x,z) = -\frac{e^2}{\left((x^2+z^2)^{\alpha/2} + \beta r_B^{\alpha}\right)^{1/\alpha}}, \tag{12}$$

where α and β are the parameters related by the condition of the equality between the ground-state energy and the atom ionization potential. Figure 1(b) shows this relation for the H atom. The generalization of the 1D soft-core potential to the 2D case for the H atom is [31]:

$$V_{\rm 2D}(x,z) = -\frac{e^2}{\sqrt{x^2+z^2+0.64r_B^2}}. \tag{13}$$

Like in the 1D case, we propose to use the 2D pliant-core potential [Eq. (12) with $\alpha = 3/2$] and the 2D supersolid-core potential [Eq. (12) with $\alpha = 1/2$] in the calculations of the HHG spectra and RCD, respectively. For the H atom, the 2D pliant-core potential is

$$V_{\rm 2D}(x,z) = -\frac{e^2}{\left((x^2+z^2)^{3/4} + 0.52r_B^{3/2}\right)^{2/3}}, \tag{14}$$

and the 2D supersolid-core potential is

$$V_{\rm 2D}(x,z) = -\frac{e^2}{\left((x^2+z^2)^{1/4} + 0.24r_B^{1/2}\right)^{2}}. \tag{15}$$

In subsequent numerical calculations, to make the study more comprehensive, we also consider the 2D solid-core potential which is the generalization of 1D solid-core potential (8) to the 2D space:

$$V_{\rm 2D}(x,z) = -\frac{e^2}{\sqrt{x^2+z^2+0.39r_B}}. \tag{16}$$

In Table I we present the calculated values of the parameter β for 2D pliant-core and supersolid-core potentials, which correspond to different noble-gas atoms. Note that when one solves the TDSE numerically by using spatial computation grid, the value of the ground-state energy in the potential can depend slightly on the spatial step of the grid and the location of grid nodes relative to the point of origin. This fact can be rather important for the case of 3D Coulomb potential as well as for the 1D and 2D supersolid-core potentials since they are very sharp near the point of origin. Possible disagreement between the value of the ground-state energy in numerical calculations and the experimentally measured value of ionization potential arising from the finite size of the spatial step can be eliminated by more fine adjustment of the parameter β.

IV. NUMERICAL RESULTS

In this section, we present the results of using the 1D and 2D models of the H atom for calculating the HHG spectrum and RCD in a wide range of laser-pulse parameters and compare them with the results given by the 3D approach. The time dependence of the electric field $E(t)$ of the laser pulse is specified as

$$\begin{aligned} E(t) &= \frac{1}{\omega_L}\frac{\partial A}{\partial t}, \\ A(t) &= E_0 \sin(\omega_L t + \varphi_{\rm CEP}) \exp\left(-(2\ln 2)\frac{t^2}{\tau_p^2}\right), \end{aligned} \tag{17}$$

where ω_L is the carrier frequency, E_0 is the envelope maximum, $\varphi_{\rm CEP}$ is CEP, and τ_p is the pulse duration (the intensity full-width at half-maximum, FWHM). Setting the field as Eq. (17) ensures that the zeroth harmonic in the electric-field spectrum is equal to zero.

A. Methods

The 3D TDSE is solved in the cylindrical system of coordinates (ρ, θ, z). The use of cylindrical coordinates in the case when the laser pulse is linearly polarized and the electron is initially in the s state makes it possible to reduce the computation time significantly compared with the solution in the Cartesian coordinates. The 3D TDSE in the cylindrical coordinates is written as follows:

$$i\hbar\frac{\partial\psi(\rho,z,t)}{\partial t} = -\left[\frac{\hbar^2}{2m}\left(\frac{\partial^2}{\partial\rho^2}+\frac{1}{\rho}\frac{\partial}{\partial\rho}+\frac{\partial^2}{\partial z^2}\right) + \frac{e^2}{\sqrt{\rho^2+z^2}}+eE(t)z\right]\psi(\rho,z,t). \quad (18)$$

The numerical solution of the 1D, 2D, and 3D TDSEs is found by the split-step method [78]. To transform the wave function from the coordinate representation into the momentum one (and back), the fast Fourier transform (FFT) is used in the 1D and 2D problems. In the 3D problem, FFT with respect to z and the discrete Fourier-Bessel transform with respect to ρ are used. The calculations are performed in the regions $-z_{\max} \leqslant z \leqslant z_{\max}$ (1D TDSE), $-z_{\max} \leqslant z \leqslant z_{\max}$, $-x_{\max} \leqslant x \leqslant x_{\max}$ (2D TDSE), and $-z_{\max} \leqslant z \leqslant z_{\max}$, $0 \leqslant \rho \leqslant \rho_{\max}$ (3D TDSE). To avoid reflections from the boundaries of the computation domain, absorption of the wave function [79] is used for $\tilde{z} \leqslant |z| \leqslant z_{\max}$, $\tilde{x} \leqslant |x| \leqslant x_{\max}$, and $\tilde{\rho} \leqslant \rho \leqslant \rho_{\max}$ following the method proposed in Ref. [80]. The integration with respect to time t is performed for $-t_{\max} \leqslant t \leqslant t_{\max}$ with the time step $\mathbf{\Delta}t$. The following parameters ensuring the required accuracy of the calculations are used: $z_{\max} = 4r_{\rm osc}$, $\tilde{z} = 3r_{\rm osc}$, $x_{\max} = 60r_B$, $\tilde{x} = 40r_B$, $\rho_{\max} = 60r_B$, $\tilde{\rho} = 40r_B$, $t_{\max} = 4\tau_p$, $\mathbf{\Delta}t = 0.02t_a$, where $r_{\rm osc} = |eE_0/m\omega_L^2|$ is the oscillatory radius of the electron corresponding to the peak amplitude of the electric field, and $t_a = 2.42 \times 10^{-17}$s is the atomic unit of time. For 1D and 2D TDSEs, the spatial steps are $\mathbf{\Delta}z = 0.1r_B$ and $\mathbf{\Delta}z = \mathbf{\Delta}x = 0.2r_B$, respectively. When the 3D TDSE is solved, the uniform grid with respect to z is used with $\mathbf{\Delta}z = 0.25r_B$, while the grid nodes with respect to ρ are placed nonuniformly. The grid becomes denser toward $\rho = 0$, and the total number of nodes is set equal to $N_\rho = 500$.

B. HHG spectrum

Consider first a laser pulse with parameters close to those used in Ref. [49]. Let the laser pulse contain one cycle of the optical field ($K = \omega_L\tau_p/2\pi = 1$, $\tau_p = 2.67$ fs) with the central wavelength $\lambda_L = 800$ nm and the intensity $I = 1.14 \times 10^{15}$ W/cm^2 ($I = cE_0^2/8\pi$ where c is the velocity of light). The HHG spectra $|a_\omega|^2$ found with the 1D model potentials, as well as by an exact 3D calculation are shown in Fig. 2. It is seen that, in agreement with Ref. [49], the HHG spectrum obtained by the use of the 1D solid-core potential is close to the spectrum obtained by the 3D calculation, while for the 1D soft-core and pliant-core potentials the spectral intensities are underestimated by several orders of magnitude. However, as we will show below, the performance of the solid-core potential is typically not as good as in this particular case.

Let us consider a laser pulse with longer duration ($K = 1.5$, $\tau_p = 4$ fs) and lower intensity $I = 5 \times 10^{14}$ W/cm^2 [see Fig. 3(a)]. For these parameters, the best agreement with

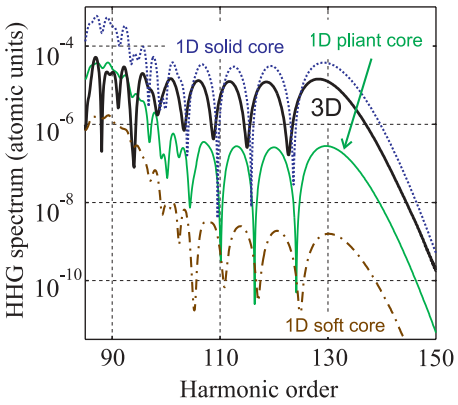

FIG. 2. (Color online) The HHG spectrum found by solving the 1D TDSE with different model potentials and by solving the 3D TDSE (thick curve). Laser pulse has the duration $\tau_p = 2.67$ fs, the intensity $I = 1.14 \times 10^{15}$ W/cm^2 ($E_0 = 0.18E_a$), the wavelength $\lambda_L = 800$ nm, and the carrier-envelope phase $\varphi_{\rm CEP} = 0$. (Dotted curve) The solution of the 1D TDSE with solid-core potential, (thin solid curve) with pliant-core potential, and (dash-and-dotted curve) with soft-core potential.

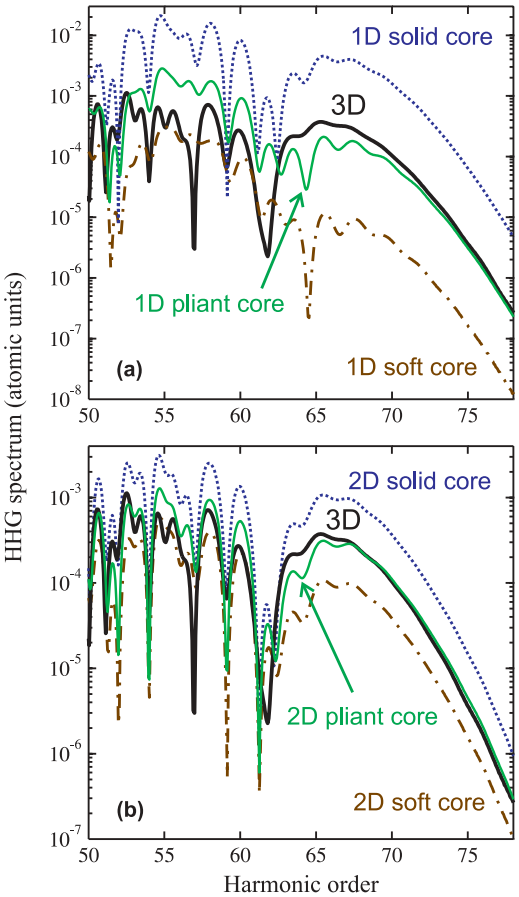

FIG. 3. (Color online) The HHG spectrum found by solving (a) the 1D and (b) the 2D TDSE with different model potentials and by solving the 3D TDSE (thick curve). Laser pulse has the duration $\tau_p = 4$ fs, the intensity $I = 5 \times 10^{14}$ W/cm^2, the wavelength $\lambda_L = 800$ nm, and CEP $\varphi_{\rm CEP} = 0$. (Dotted curves) The results obtained with solid-core potentials, (dash-and-dotted curves) with soft-core potentials, and (thin solid curves) with our proposed pliant-core potentials.

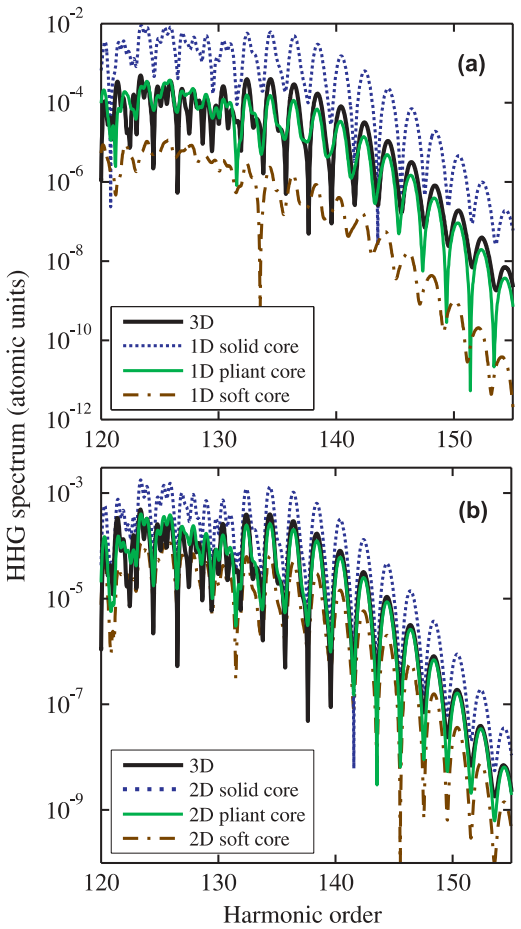

FIG. 4. (Color online) Same as shown in Fig. 3 but for the wavelength $\lambda_L = 1200$ nm, the pulse duration $\tau_p = 20$ fs, and the intensity $I = 3 \times 10^{14}$ W/cm^2.

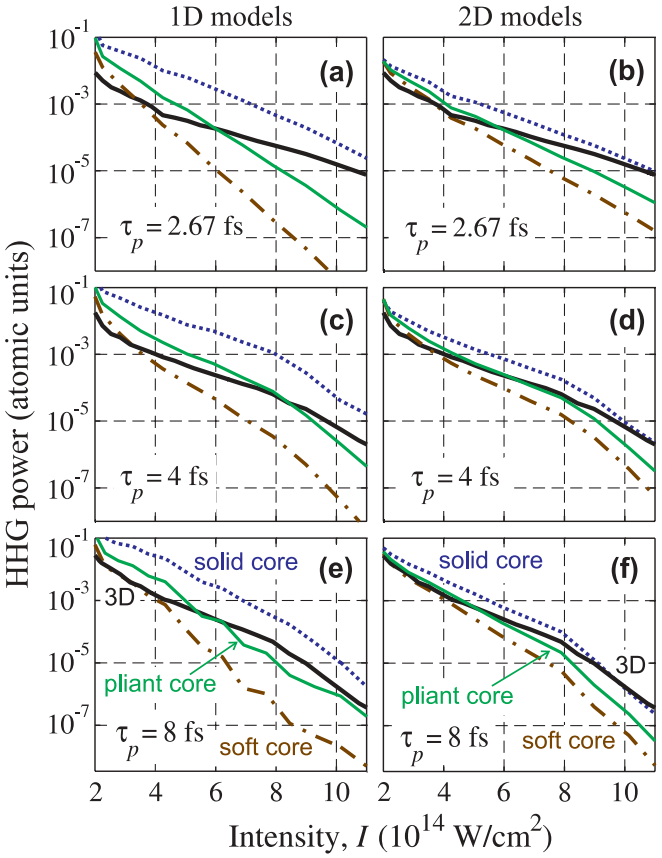

FIG. 5. (Color online) Integrated HHG spectrum over the interval at the edge of plateau [Eq. (19) for $\hbar\Delta\omega = 38.7$ eV] as a function of the laser pulse intensity I for the wavelength $\lambda_L = 800$ nm, CEP $\varphi_{\rm CEP} = 0$, and different pulse durations: (a and b) $\tau_p = 2.67$ fs, (c and d) $\tau_p = 4$ fs, and (e and f) $\tau_p = 8$ fs. Results are obtained on the basis of (a, c, and e) the 1D and (b, d, and f) the 2D TDSE solution by using the soft-core (dash-and-dotted curves), solid-core (dotted curves), and pliant-core (thin solid curves) potentials, as well as on the basis of the 3D TDSE (thick solid curves).

the exact 3D solution is achieved when using the proposed 1D pliant-core potential, whereas the use of the 1D solid-core potential overestimates the spectral intensity near the cutoff by an order of magnitude, and the use of the 1D soft-core potential underestimates this value even more. This regularity is observed also for the HHG spectra calculated with the 2D TDSE [Fig. 3(b)]. For a higher laser wavelength, $\lambda_L = 1200$ nm, and greater number of field cycles, $K = 5$ ($\tau_p = 20$ fs), the HHG spectra calculated using pliant-core potentials also agree well with the results of the 3D calculations (see Fig. 4).

For a more detailed comparison of the HHG spectra obtained using different potentials, we calculate the value of the HHG power (the integral of the spectral intensity $|a_\omega|^2$ over the specified spectral interval) for different values of the intensity, duration, and wavelength of the laser pulse. First, we consider the integral of $|a_\omega|^2$ over the spectral interval at the cutoff region:

$$P_{\Delta\omega} = \int_{\omega_c - \Delta\omega}^{\omega_c + \Delta\omega} |a_\omega|^2 d\omega, \tag{19}$$

where $\omega_c = (I_p + 3.17U_p)/\hbar$ is the cutoff frequency [16,81], $U_p = e^2E_0^2/(4m\omega_L^2)$ is the maximum ponderomotive potential, and $\Delta\omega$ is the half-width of the spectral interval, over which the integration is performed. Figure 5 shows the dependences of the HHG power on the laser peak intensity I for $\lambda_L = 800$ nm and different values of the pulse duration τ_p. We set $\hbar\Delta\omega = 25\hbar\omega_L \approx 38.7$ eV and specify CEP as $\varphi_{\rm CEP} = 0$, since we found that the change in CEP and small change in $\Delta\omega$ have almost no effect on the calculated dependence $P_{\Delta\omega}(I)$. One can see that the 1D solid-core potential gives most accurate results for $P_{\Delta\omega}$ only for short durations, $\tau_p \sim 2.67$ fs, and high intensities, $I \geqslant 10^{15}$ W/cm^2. For lower intensities and longer pulse durations the HHG power calculated by using the 1D solid-core potential is strongly overestimated. It agrees well also with the results shown in Figs. 2 and 3. For $I \geqslant 5 \times 10^{14}$ W/cm^2 and $\tau_p \geqslant 4$ fs the most accurate is the 1D pliant-core potential. In the 2D case, at high intensities, $I \geqslant 10^{15}$ W/cm^2, the 2D solid-core potential is most accurate for all considered durations, $\tau_p \sim 3$–8 fs, while at lower intensities, $I \sim (4$–$8) \times 10^{14}$ W/cm^2, the 2D pliant-core potential is the most accurate.

We also studied the dependences of the HHG power $P_{\Delta\omega}$ on the central wavelength λ_L of the laser pulse. The results obtained for a fixed number $K = 5$ of field cycles and the intensity $I = 3 \times 10^{14}$ W/cm^2 are shown in Fig. 6. The HHG

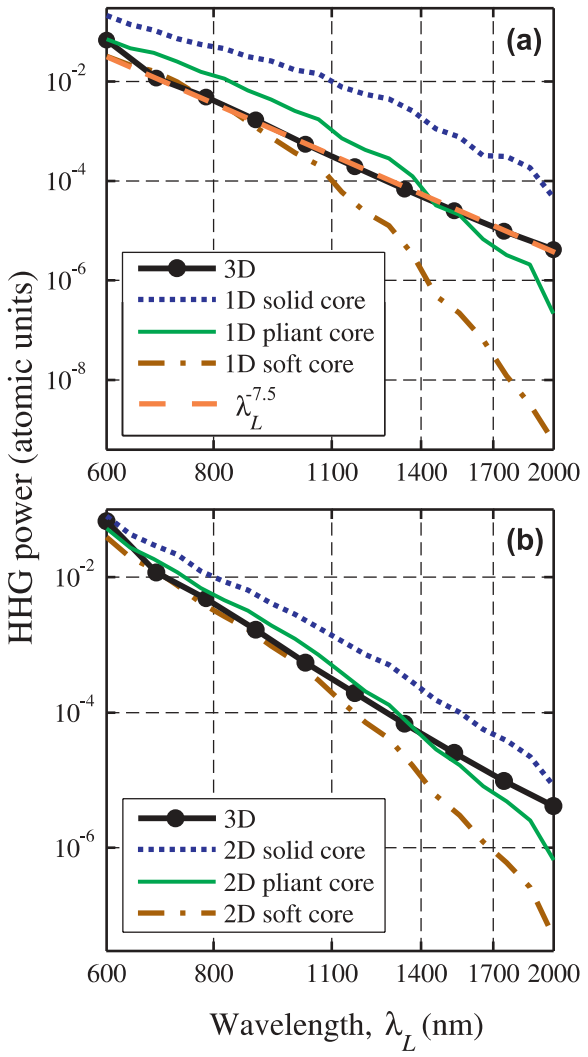

FIG. 6. (Color online) Dependence of the HHG power [Eq. (19) for $\hbar\Delta\omega = 32$ eV] on the laser pulse central wavelength λ_L. The laser pulse has the intensity $I = 3 \times 10^{14}$ W/cm^2, CEP $\varphi_{\rm CEP} = 0$, and contains five cycles at FWHM. Results are obtained on the basis of solving (a) the 1D TDSE and (b) the 2D TDSE using the soft-core (dash-and-dotted curves), solid-core (dotted curves), and pliant-core (thin solid curves) potentials. Results obtained from the 3D TDSE are shown by thick solid curves. The dashed line corresponds to the power law $\lambda_L^{-7.5}$.

power found by solving the 3D TDSE follows the power law $\lambda_L^{-7.5}$, which agrees well with the analytical result λ_L^{-7} obtained recently [62]. When reduced-dimensionality models are used, the value of $P_{\Delta\omega}$ in the long-wavelength range decreases with λ_L stronger than by the power law. However, it should be noted that the use of the 1D pliant-core potential yields the best agreement with the results of the 3D calculations in a wide range of wavelengths. For the considered values of the pulse intensity and duration, this interval is 1100 nm $\leqslant \lambda_L \leqslant$ 2000 nm. When using the 1D solid-core potential, the value of $P_{\Delta\omega}$ is overestimated by more than an order of magnitude in the entire considered range of λ_L. When the 1D soft-core potential is used, the value of $P_{\Delta\omega}$ corresponds approximately with the exact value at $\lambda_L = 800$ nm and deviates from it fast as λ_L grows. For $\lambda_L = 1600$ nm, it is underestimated by more than two orders of magnitude. In the 2D case, the curves $P_{\Delta\omega}(\lambda_L)$ lie generally much closer to the curve found by solving the 3D problem. The curve $P_{\Delta\omega}(\lambda_L)$ calculated using the 2D pliant-core potential agrees well with the exact curve in the wavelength range $\lambda_L \sim$ 700–1800 nm.

Thus, the 1D and 2D pliant-core potentials, which we propose, give high accuracy when spectral HHG intensities are calculated near the cutoff. However, it is also of great interest to study the λ_L scaling of the integral of the spectral intensity $|a_\omega|^2$ over a fixed frequency interval, whose position is independent of λ_L [62–67],

$$P_{\Delta\omega} = \int_{\omega_i}^{\omega_f} |a_\omega|^2 d\omega. \tag{20}$$

Our calculations show that for this definition of $P_{\Delta\omega}$, reduced-dimensionality models yield the decrease of the HHG power according to the power law, as it happens both in the 3D calculations [63–65] and in the experiments [67]. Table II lists the values for the exponent κ of the wavelength scaling law $P_{\Delta\omega} \propto \lambda_L^{-\kappa}$ obtained using reduced-dimensionality models and the 3D approach for the laser pulse parameters same as in the previous paragraph; the integration was performed over the harmonic energy interval between $\hbar\omega_i = 25$ eV and $\hbar\omega_f = 65$ eV. In the case of reduced-dimensionality models, the exponent κ is almost independent of the potential used. When the dimensionality of the problem is increased by unity, κ increases by approximately 0.5–0.7 rather than by unity, as one could expect reasoning from the analysis of the influence of spreading of the ionized wave packet on the values of spectral HHG intensities [81]. This proves that the wave-packet spreading is not the only important factor that determines the dependences of the plateau height on the dimensionality of the problem and on the laser wavelength. The value of κ found by solving the 3D TDSE is equal to 4.3, approximately. Some difference of this value from $\kappa = 4.8$ reported in Ref. [64] can be due to the fact that our calculations were performed for a different shape of the electric-field envelope, a higher pulse intensity, and a wider spectral interval $\Delta\omega = \omega_f - \omega_i$. The significant difference in the value of κ compared with that obtained experimentally ($\kappa = 6.3 - 6.5$) [67] is caused, on the one hand, by the fact that the experiment in Ref. [67] was made in Xe and Kr, whereas our calculations described herein were performed for the H atom. As it was shown in Refs. [64,65], the wavelength scaling of the HHG power can differ significantly for different atoms. On the other hand, in many articles it has already been noted that in experiments, the decrement of the harmonic yield with λ_L turns out to be

TABLE II. Exponent κ of the wavelength scaling law $P_{\Delta\omega} \propto \lambda_L^{-\kappa}$ [Eq. (20) for $\hbar\omega_i = 25$ eV and $\hbar\omega_f = 65$ eV] found by solving the 1D and 2D TDSE with different model potentials and by solving the 3D TDSE with the Coulomb potential. The laser pulse contains 5 cycles at FWHM and has the intensity $I = 3 \times 10^{14}$ W/cm^2.

Dimension	Model potentials			3D Coulomb potential
	Soft core	Pliant core	Solid core	
1D	3.0	3.1	3.2	4.3
2D	3.7	3.75	3.8	

much higher than that predicted theoretically. This takes place even despite the fact that the experiments in Ref. [67] were performed under the conditions, when the collective effects should not play any significant role. This fact has not been given any solid explanation yet.

C. Residual current density

Below we present the results of calculating RCD. For the normalization of the value of j_{RCD}, we use the maximum oscillatory-current density, $j_{\mathrm{osc}} = eN_g V_{\mathrm{osc}} = e^2 N_g E_0/m\omega_L$, where V_{osc} is the oscillatory velocity of the electron corresponding to the peak amplitude of the electric field. The normalized RCD $j_{\mathrm{norm}} = j_{\mathrm{RCD}}/j_{\mathrm{osc}}$ found in this way is a dimensionless factor, which characterizes the efficiency of generation of RCD [7,12,13]. Note that j_{norm} is independent of the initial gas density N_g and is related to the value of the zeroth harmonic a_0 of the dipole acceleration as $j_{\mathrm{norm}} = (m\omega_L/eE_0)a_0$. We study the dependences $j_{\mathrm{norm}}(\varphi_{\mathrm{CEP}}) = -j_{\mathrm{norm}}(\varphi_{\mathrm{CEP}} + \pi)$ of the normalized RCD on CEP for different fixed pulse durations and intensities. Accurate calculation of these dependences can be important for the monitoring of CEP of few-cycle laser pulses by means of detection of the THz waves radiated by the laser-produced plasma. Of greatest significance is to find the exact value of optimal CEP φ_{opt} at which the absolute value of j_{norm} has a maximum, as well as the maximum normalized RCD $j_{\mathrm{max}} = |j_{\mathrm{norm}}(\varphi_{\mathrm{opt}})|$ itself [12,13].

Figure 7 shows the dependencies $j_{\mathrm{norm}}(\varphi_{\mathrm{CEP}})$ calculated for the pulses with $\tau_p = 4$ fs, $\lambda_L = 800$ nm, and various peak intensities. One can see that the best agreement with the 3D calculations is reached when the proposed 1D and 2D supersolid-core potentials are used. For all considered values of laser intensity, the use of supersolid-core potentials yields almost exact values of the maximum normalized RCD j_{max}. The optimal CEP φ_{opt}, which is found from the calculations involving the supersolid-core potentials, also agrees with that found by the 3D calculation for considered values of the intensity. Searching for the dependences $j_{\mathrm{norm}}(\varphi_{\mathrm{CEP}})$ by means of the calculations involving the other 1D and 2D model potentials results in a strong overestimation of j_{max} compared with the 3D calculation. For low laser intensity, this overestimation amounts to several times. The optimal CEP found by using the soft-core and solid-core potentials agrees well with its value found by the 3D calculation at sufficiently low laser intensities and starts to differ at higher intensities, $I \geqslant 10^{14}$ W/cm^2.

Figure 8 shows the dependences $j_{\mathrm{norm}}(\varphi_{\mathrm{CEP}})$ for longer pulse duration, $\tau_p = 6$ fs. Calculations of RCD using the 1D and 2D supersolid-core potentials have high accuracy at high intensities, $I \geqslant 8 \times 10^{14}$ W/cm^2. At lower intensities, the use of supersolid-core potentials leads to significant deviations from the 3D calculations for φ_{opt} and j_{max}. The results of calculations of $j_{\mathrm{norm}}(\varphi_{\mathrm{CEP}})$ using the other model potentials differ strongly from the results of the 3D calculations for all considered intensities. Note that for this duration of the laser pulse the dependences $j_{\mathrm{norm}}(\varphi_{\mathrm{CEP}})$ have a jagged shape with several maxima at $0 \leqslant \varphi_{\mathrm{CEP}} < \pi$. This is connected with the fact that when the duration of the laser pulse is rather long, the RCD value is strongly influenced by the processes of the electron scattering on and recombination with the parent

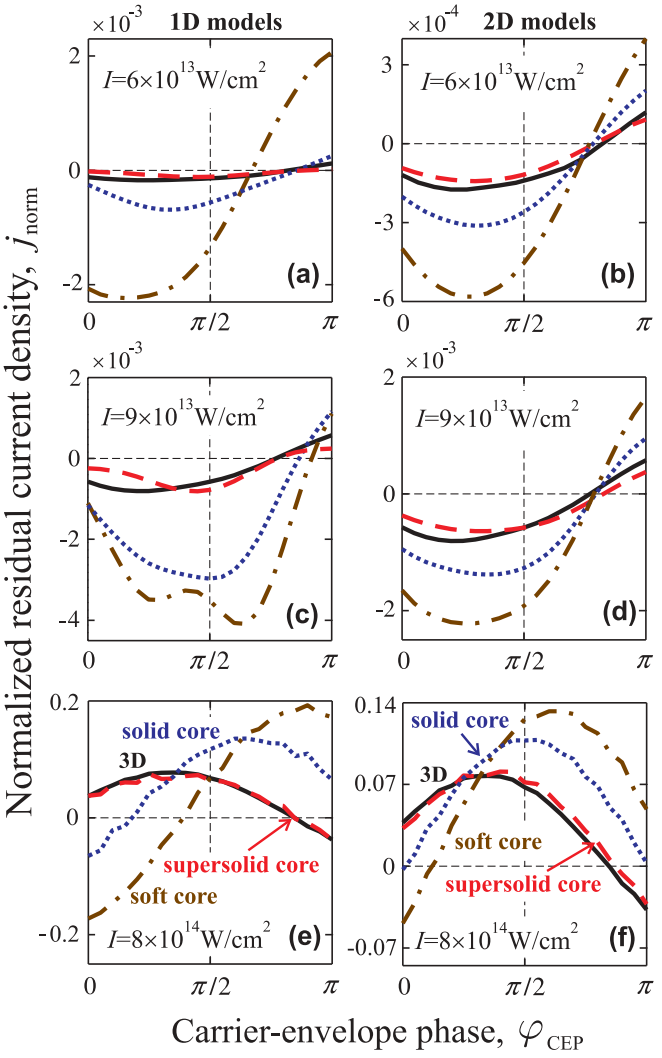

FIG. 7. (Color online) Normalized residual current density $j_{\mathrm{norm}} = j_{\mathrm{RCD}}/j_{\mathrm{osc}}$ as a function of the carrier-envelope phase φ_{CEP} for a laser pulse with the duration $\tau_p = 4$ fs, the wavelength $\lambda_L = 800$ nm, and different values of the intensity: (a and b) $I = 6 \times 10^{13}$ W/cm^2, (c and d) $I = 9 \times 10^{13}$ W/cm^2, and (e and f) $I = 8 \times 10^{14}$ W/cm^2. Here, $j_{\mathrm{osc}} = e^2 E_0 N_g/(m\omega_L)$ is the maximum oscillatory-current density. Results are obtained on the basis of (a, c, and e) the 1D and (b, d, and f) the 2D TDSE solution by using the soft-core (dash-and-dotted curves), solid-core (dotted curves), and supersolid-core (dashed curves) potentials, as well as the 3D TDSE solution (solid curves).

ion [12]. The influence of these processes is most significant for the 1D models, since the scattering and recombination cross sections are the highest in the 1D problem (see also Sec. VI).

V. PROBABILITIES OF STATIC-FIELD IONIZATION AND RECOMBINATION AMPLITUDES

A. Probabilities of static-field ionization

Despite the same ground-state energy, different model potentials give different rates of the atom ionization. Let us show this by calculating the probability of atom ionization in a static electric field. We consider a wide range of electric-field

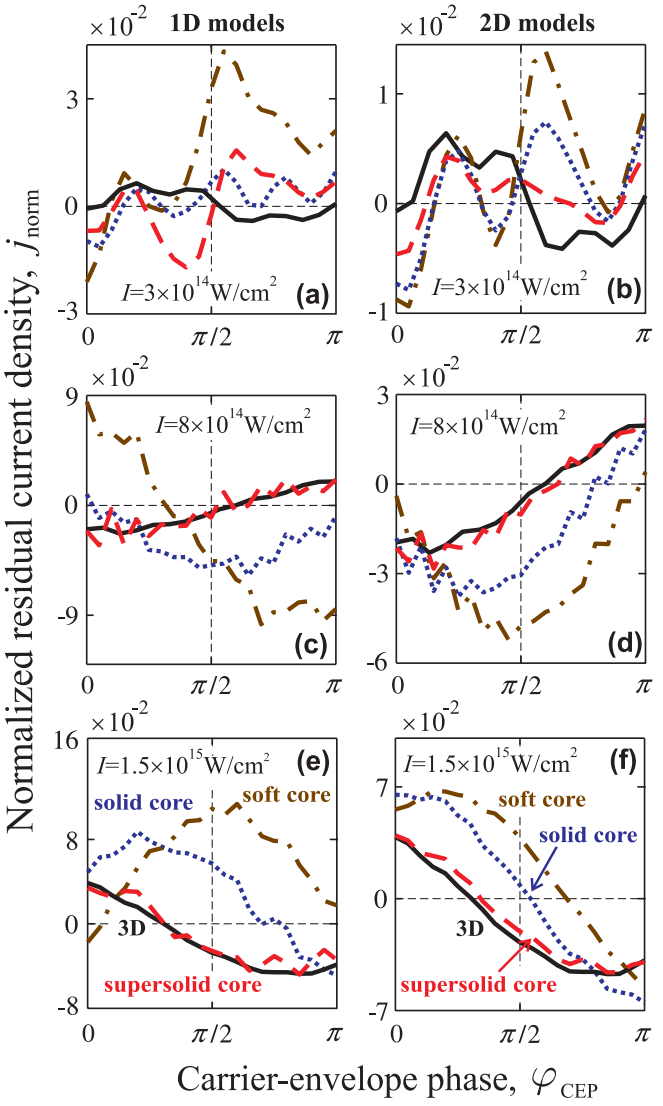

FIG. 8. (Color online) Same as shown in Fig. 7 but for the pulse duration $\tau_p = 6$ fs and intensities (a and b) $I = 3 \times 10^{14}$ W/cm^2, (c and d) $I = 8 \times 10^{14}$ W/cm^2, and (e and f) $I = 1.5 \times 10^{15}$ W/cm^2.

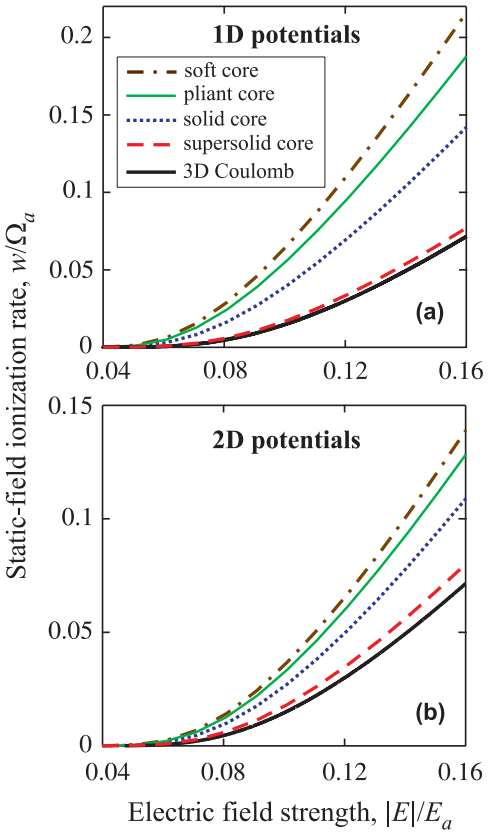

FIG. 9. (Color online) Static-field ionization rate w (in atomic-frequency units Ω_a) as function of the external electrostatic field E (in atomic-field units E_a) for (a) the 1D and (b) the 2D model potentials, as well as for the 3D Coulomb potential (thick solid curve). Dependences $w(|E|)$ calculated for soft-core potentials (dash-and-dotted curves), pliant-core potentials (thin solid curves), solid-core potentials (dotted curves), and supersolid-core potentials (dashed curves).

strengths, $E < 0.16E_a$, which includes the ranges relevant to both the tunneling regime and the above-barrier regime of ionization.

We calculate the probability w of atom ionization from the ground state in the static electric field per time unit by solving the time-independent Schrödinger equation

$$\hat{H}\psi = \varepsilon\psi, \tag{21}$$

with the Hamiltonian operator

$$\hat{H} = -\frac{\hbar^2}{2m}\nabla^2 + V(r) - eEz. \tag{22}$$

We find the spectrum of complex eigenvalues ε of the Hamiltonian operator with the boundary conditions in the form of the radiation condition for the wave function in the direction of the electric field. The sought-for spectrum is continuous; however, there is a set of long-living quasistationary states [82]. The energy spectrum of these states consists of a series of broadened quasidiscrete levels whose widths are associated with their lifetimes. The probability of atom ionization per time unit is proportional to the imaginary part of ε [83]. When an electron is in the ground state initially, $w = |2\mathrm{Im}(\varepsilon_0)/\hbar|$, where ε_0 is the complex energy of the lowest quasistationary state. To find the dependence $w(|E|)$, we use the method of complex rotation of coordinates [83].

Figure 9 shows the ionization rates $w(|E|)$ calculated for the 1D and 2D model potentials as well as for the 3D Coulomb potential. It is seen that rates for different 1D and 2D potentials differ rather strongly from each other, despite the fact that all these potentials have equal ground-state energies and the same asymptotic behavior far from the ion. The ionization rates for the soft-core, solid-core, and pliant-core potentials are significantly higher than that for the 3D Coulomb potential. The ionization rates calculated for the supersolid-core potentials coincide almost precisely with that for the 3D Coulomb potential in the entire considered range of electric field values. As follows from results of the calculation, this agreement holds with high accuracy for even lower and higher electric fields.

A strong difference of the probability of the static-field ionization for different model potentials is associated with

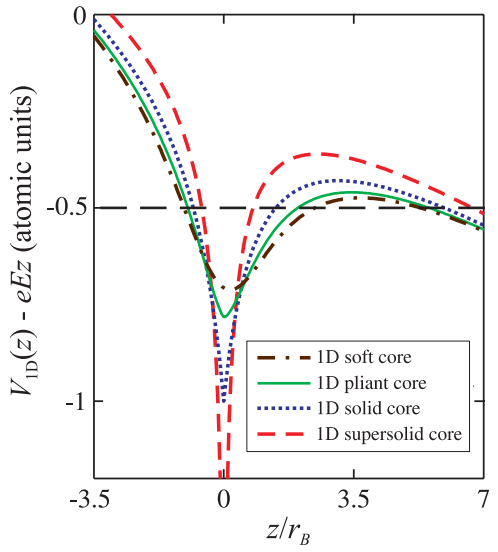

FIG. 10. (Color online) The total electric potential created by the parent ion and the external electric field for different 1D models of the H atom and the electric-field strength $|E| = 0.06E_a$. The dashed line denotes the energy of the field-free ground state in the potentials.

strong difference of these potentials near the point of origin. The potential barriers, which the electron has to overcome in order to be detached from the ion, have different widths and heights. This is clearly seen in Fig. 10, which shows the total electric potential created by the parent ion and the external electric field for the 1D models.

B. Recombination amplitudes

Here we consider the stage of the recombination of the electron with the parent ion. We calculate recombination amplitude as a function of the kinetic energy of the recolliding photoelectron. The amplitude of electron recombination into the ground state ψ_0 of the atom is determined as [49,51]

$$A_{\rm rec} = \langle \psi_0 | \frac{\partial V(r)}{\partial z} | \psi_p \rangle. \tag{23}$$

Here, $\psi_p \propto \exp(ipz/\hbar)$ is a plane wave that describes an electron moving along the z axis and having the kinetic energy $E_{\rm kin} = p^2/2m$. We normalize the function ψ_0 to unity, and the function ψ_p, to the momentum delta function. When such normalizations are used, the recombination amplitudes for the cases of 1D and 2D potentials are

$$A_{\rm 1D} = \frac{1}{\sqrt{2\pi}} \int \exp\left(\frac{ipz}{\hbar}\right) \psi_0^*(z) \frac{\partial V_{\rm 1D}(z)}{\partial z} dz \tag{24}$$

and

$$A_{\rm 2D} = \frac{1}{2\pi} \int \exp\left(\frac{ipz}{\hbar}\right) \psi_0^*(x,z) \frac{\partial V_{\rm 2D}(x,z)}{\partial z} dx dz, \tag{25}$$

respectively. For the exact Coulomb potential, $V_{\rm 3D}(r) = -e^2/r$, the recombination amplitude is calculated analytically [49]:

$$A_{\rm 3D} = \frac{i\sqrt{2}e^2\hbar}{\pi r_B^{1/2}} \frac{r_B p - \hbar \arctan(r_B p/\hbar)}{(r_B p)^2}. \tag{26}$$

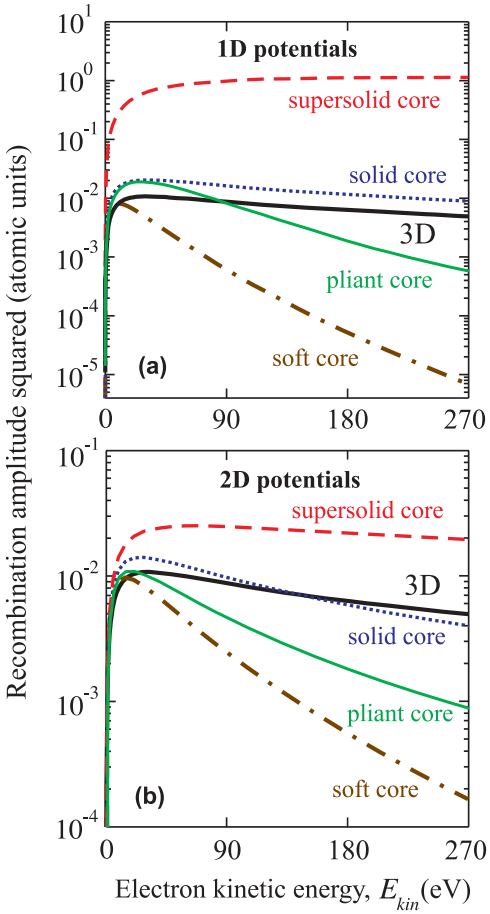

FIG. 11. (Color online) Recombination amplitudes [Eqs. (24)–(26)] squared as functions of the kinetic energy $E_{\rm kin}$ of the recolliding electron for (a) the 1D and (b) the 2D model potentials, as well as for the 3D Coulomb potential (thick solid curve). (Dashed curves) The results obtained for supersolid-core potentials, (dotted curves) solid-core potentials, (thin solid curves) pliant-core potentials, and (dash-dotted curves) soft-core potentials.

Note that the recombination amplitudes (24)–(26) have different dimensionalities. Therefore, these values can be correlated meaningfully only when their scaling with $E_{\rm kin}$ is compared.

Dependences $|A_{\rm 1D}|^2(E_{\rm kin})$, $|A_{\rm 2D}|^2(E_{\rm kin})$, and $|A_{\rm 3D}|^2(E_{\rm kin})$ are shown in Fig. 11. The recombination amplitudes are decreasing functions of $E_{\rm kin}$ for $E_{\rm kin} \gg I_p$ with the decrement strongly dependent on the particular model potential used in the problem. For the 1D and 2D soft-core potentials, which are the smoothest at the point of origin, the decrements of the functions $|A_{\rm 1D}|^2(E_{\rm kin})$ and $|A_{\rm 2D}|^2(E_{\rm kin})$ are highest. For the pliant-core potentials, the recombination amplitude decreases more slowly. For the solid-core potentials, the scaling of the recombination amplitude is similar to that for the 3D case. Finally, the decrement of the recombination amplitude is the slowest for the supersolid-core potentials, which are sharpest at the ion location point.

VI. DISCUSSION

Consider the results of calculating the HHG spectra. In Sec. IV, we found that for a rather wide range of laser pulse parameters such as the pulse duration (∼2–5 cycles at FWHM), intensity ($\sim 10^{14}-10^{15}$ W/cm^2), and wavelength (∼0.8–2 μm), the best agreement with the 3D calculations of the HHG spectra near the cutoff is achieved when the proposed pliant-core potentials are used. This result may seem rather surprising, since, as it was shown in Sec. V B, the solid-core potentials yield a more accurate scaling of the recombination amplitude with the electron kinetic energy, as compared with the pliant-core potentials. Nevertheless, the use of the solid-core potentials leads to an overestimation of spectral intensities near the cutoff in the nearly entire range of the considered intensities, up to 10^{15} W/cm^2. In order to explain this fact, one should take into account that the harmonic yield is strongly influenced by the factors related to the electron dynamics at all three stages [16] of the HHG process, and not only at its third, final stage, namely the recombination of the electron with the parent ion, which is the focus of attention in Ref. [49]. At the first stage of the HHG process, a great part is played by the probability of atom ionization per time unit. Its value affects strongly both the probability density of the returning wave packet and the atomic ground-state population at the recollision moment. At the second stage of the HHG process (motion of the electron in continuum), the main factor which influences the HHG yield is wave-function spreading. Additional factor that can play a significant part at the second stage is the Coulomb focusing of the wave packet [50,84], which results in an increase of the probability density of the recombining wave packet, including the contribution made into the HHG yield by the electron trajectories with multiple returns. Generally speaking, the influence of each of these factors on the harmonic yield depends on both the dimensionality of the problem and the shape of the ion potential. When the pliant-core potentials proposed by us are used, the result of the interplay between the above-mentioned factors is that the spectral HHG intensities, as well as the wavelength scaling of the HHG power at the cutoff region, agree well with the corresponding values found by solving the 3D problem. The range of the laser pulse parameters for which this agreement takes place may seem not too wide, but this is indeed the range which is in fact optimal for HHG and attosecond pulse production.

The use of the supersolid-core potential yields the RCD values agreeing well with those for the 3D case and gives much higher accuracy than the calculations within other 1D and 2D models. This does not hold only at low intensities and long durations of the laser pulse. At such parameters, first, the multiphoton ionization dominates over the tunneling ionization [85] and, second, the evolution of the electron wave packet in continuum is influenced greatly by the processes of electron scattering on and recombination with the parent ion [12,13]. Reduced-dimensionality models are unable of describing these processes with the required accuracy, which yields the errors of RCD determination. At high intensities of laser pulses, atom ionization has the tunneling character and the influence of these processes on the electron dynamics is weaker. When the 1D and 2D supersolid-core potentials are used, the tunneling ionization is modeled with high accuracy, which yields correct results for RCD.

VII. CONCLUSIONS

We have considered two strong-field phenomena caused by intense ultrashort laser pulses, which can be observed under similar experimental conditions. The first phenomenon is generation of high-order harmonics of the driving laser field, which is interesting from the viewpoint of its use for the generation of extreme UV and soft-x-ray radiation and, specifically, attosecond pulses. The second phenomenon is the generation of the residual current density in the plasma produced by a few-cycle laser pulse, which can lead to the generation of low-frequency radiation including THz waves.

We proposed new reduced-dimensionality models to find solutions of the TDSE for the H atom and various noble-gas atoms irradiated by ultrashort laser pulses. The reduced-dimensionality models allow one to reduce significantly the time required for the numerical TDSE solution as compared with the full-dimensionality case, while retaining the quantum description of all stages of the electron dynamics in its entirety.

To find the high-frequency part of the harmonic spectra, the proposed 1D and 2D model *pliant-core* potentials for the H atom are given by Eqs. (10) and (14), respectively. To calculate the RCD of free electrons, the model *supersolid-core* potentials for the H atom are given by Eqs. (11) and (15). An advantage of the pliant-core potentials over the model potentials proposed earlier is that their use for calculations of the HHG spectrum yields the results agreeing well with the results of 3D simulation in the range of laser pulse parameters interesting to the experimentalists from the viewpoint of the generation of the extreme UV radiation and attosecond pulses. The use of the proposed 1D and 2D supersolid-core potentials for RCD calculations results in a qualitatively good agreement with the 3D calculation for almost all values of the intensity and duration of laser pulses, which have been considered here. We expect that, specifically, the use of the proposed 1D and 2D supersolid-core potentials will allow one to perform high-accuracy calculations of RCD excitation in the THz generation schemes, which use mixing of the fundamental and second harmonics of the laser pulse [86–88] and are discussed actively now.

The values of spectral intensities of higher-order harmonics are determined by three main factors, namely ionization rate, transverse spreading of the electron wave packet as it moves in the continuum, and electron-ion recombination amplitude. Despite the fact that the proposed 1D and 2D pliant-core potentials do not yield accurate results for calculations of each of the above-mentioned factors individually, the use of these models for the description of the entire HHG process allows one to obtain much more accurate results in a rather wide range of laser pulse parameters as compared with the use of other 1D and 2D model potentials.

We have demonstrated that under the conditions of a sufficiently high intensity of the laser pulse, when the ionization has the tunneling character, the processes of scattering and recombination of the electron on the parent ion have little influence on the value of the generated RCD. Under

these conditions, the stage of the electron dynamics, which determines the value of RCD, is ionization. The rate of tunneling ionization yielded by the use of the proposed 1D and 2D supersolid-core potentials agrees with the ionization rate for the 3D problem with much better accuracy than when other model potentials are used.

ACKNOWLEDGMENTS

This work was supported by the Russian Foundation for Basic Research, the Presidential Council on Grants of the Russian Federation, and the Ministry of Education and Science of the Russian Federation. A.A.S. also acknowledges the support from the Dynasty Foundation.

[1] A. McPherson, G. Gibson, H. Jara, U. Johann, T. S. Luk, I. A. McIntyre, K. Boyer, and C. K. Rhodes, J. Opt. Soc. Am. B **4**, 595 (1987).
[2] M. Ferray, A. L'Huillier, X. F. Li, L. A. Lompre, G. Mainfray, and C. Manus, J. Phys. B **21**, L31 (1988).
[3] J. J. Macklin, J. D. Kmetec, and C. L. Gordon, Phys. Rev. Lett. **70**, 766 (1993).
[4] F. Krausz and M. Ivanov, Rev. Mod. Phys. **81**, 163 (2009).
[5] M. Nisoli and G. Sansone, Prog. Quantum Electron. **33**, 17 (2009).
[6] M. Kreß *et al.*, Nat. Phys. **2**, 327 (2006).
[7] V. B. Gildenburg and N. V. Vvedenskii, Phys. Rev. Lett. **98**, 245002 (2007).
[8] H.-C. Wu, J. Meyer-ter-Vehn, and Z.-M. Sheng, New J. Phys. **10**, 043001 (2008).
[9] M. Chen, A. Pukhov, X.-Y. Peng, and O. Willi, Phys. Rev. E **78**, 046406 (2008).
[10] Z.-M. Sheng, H.-C. Wu, W.-M. Wang, M. Chen, X.-G. Dong, J. Zheng, and J. Zhang, Comm. Comp. Phys. **4**, 1258 (2008).
[11] C. S. Liu and V. K. Tripathi, J. Appl. Phys. **105**, 013313 (2009).
[12] A. A. Silaev and N. V. Vvedenskii, Phys. Rev. Lett. **102**, 115005 (2009).
[13] A. A. Silaev and N. V. Vvedenskii, Phys. Scr., T **135**, 014024 (2009).
[14] K.-Y. Kim, Phys. Plasmas **16**, 056706 (2009).
[15] K. Burnett, V. C. Reed, J. Cooper, and P. L. Knight, Phys. Rev. A **45**, 3347 (1992).
[16] P. B. Corkum, Phys. Rev. Lett. **71**, 1994 (1993).
[17] M. Hentschel, R. Kienberger, Ch. Spielmann, G. A. Reider, N. Milosevic, T. Brabec, P. Corkum, U. Heinzmann, M. Drescher, and F. Krausz, Nature (London) **414**, 509 (2001).
[18] E. Goulielmakis *et al.*, Science **320**, 1614 (2008).
[19] A. Baltuška *et al.*, Nature (London) **421**, 611 (2003).
[20] J. Javanainen, J. H. Eberly, and Q. Su, Phys. Rev. A **38**, 3430 (1988).
[21] S. C. Rae, X. Chen, and K. Burnett, Phys. Rev. A **50**, 1946 (1994).
[22] J. H. Eberly, Q. Su, and J. Javanainen, Phys. Rev. Lett. **62**, 881 (1989).
[23] M. Protopapas, D. G. Lappas, C. H. Keitel, and P. L. Knight, Phys. Rev. A **53**, R2933 (1996).
[24] A. V. Kim, M. Yu. Ryabikin, and A. M. Sergeev, Phys. Usp. **42**, 54 (1999).
[25] Q. Su, J. H. Eberly, and J. Javanainen, Phys. Rev. Lett. **64**, 862 (1990).
[26] C. K. Law, Q. Su, and J. H. Eberly, Phys. Rev. A **44**, 7844 (1991).
[27] T. Seideman, M. Yu. Ivanov, and P. B. Corkum, Phys. Rev. Lett. **75**, 2819 (1995).
[28] M. Ivanov, T. Seideman, P. Corkum, F. Ilkov, and P. Dietrich, Phys. Rev. A **54**, 1541 (1996).
[29] R. Barnett and G. N. Gibson, Phys. Rev. A **59**, 4843 (1999).
[30] A. A. Babin, A. V. Kim, A. M. Kiselev, A. M. Sergeev, and A. N. Stepanov, Radiophys. Quantum Electron. **39**, 472 (1996).
[31] M. Protopapas, D. G. Lappas, and P. L. Knight, Phys. Rev. Lett. **79**, 4550 (1997).
[32] A. Patel, M. Protopapas, D. G. Lappas, and P. L. Knight, Phys. Rev. A **58**, R2652 (1998).
[33] J. R. Vázquez de Aldana and L. Roso, Opt. Express **5**, 144 (1999).
[34] N. J. Kylstra, R. A. Worthington, A. Patel, P. L. Knight, J. R. Vázquez de Aldana, and L. Roso, Phys. Rev. Lett. **85**, 1835 (2000).
[35] M. Yu. Ryabikin and A. M. Sergeev, Opt. Express **7**, 417 (2000).
[36] J. S. Parker, B. J. S. Doherty, K. T. Taylor, K. D. Schultz, C. I. Blaga, and L. F. DiMauro, Phys. Rev. Lett. **96**, 133001 (2006).
[37] M. B. Gaarde, J. L. Tate, and K. J. Schafer, J. Phys. B **41**, 132001 (2008).
[38] S. Chelkowski, A. D. Bandrauk, A. Staudte, and P. B. Corkum, Phys. Rev. A **76**, 013405 (2007).
[39] M. Lein, J. Phys. B **40**, R135 (2007).
[40] A. D. Bandrauk, S. Chelkowski, S. Kawai, and H. Lu, Phys. Rev. Lett. **101**, 153901 (2008).
[41] M. Magrakvelidze, F. He, S. De, I. Bocharova, D. Ray, U. Thumm, and I. V. Litvinyuk, Phys. Rev. A **79**, 033408 (2009).
[42] J. S. Prauzner-Bechcicki, K. Sacha, B. Eckhardt, and J. Zakrzewski, Phys. Rev. Lett. **98**, 203002 (2007).
[43] G. Camiolo, G. Castiglia, P. P. Corso, E. Fiordilino, and J. P. Marangos, Phys. Rev. A **79**, 063401 (2009).
[44] E. A. Volkova, A. M. Popov, and O. V. Tikhonova, JETP **91**, 706 (2000).
[45] P. Koval, F. Wilken, D. Bauer, and C. H. Keitel, Phys. Rev. Lett. **98**, 043904 (2007).
[46] M. A. Semina, R. A. Sergeev, and R. A. Suris, Semiconductors **42**, 1427 (2008).
[47] A. Shahbaz, C. Müller, A. Staudt, T. J. Bürvenich, and C. H. Keitel, Phys. Rev. Lett. **98**, 263901 (2007).
[48] T. Cheng, Q. Su, and R. Grobe, Laser Phys. **19**, 208 (2009).
[49] A. Gordon, R. Santra, and F. X. Kartner, Phys. Rev. A **72**, 063411 (2005).
[50] M. Yu. Ivanov, T. Brabec, and N. Burnett, Phys. Rev. A **54**, 742 (1996).
[51] A. Gordon and F. X. Kärtner, Phys. Rev. Lett. **95**, 223901 (2005).
[52] N. Rohringer, A. Gordon, and R. Santra, Phys. Rev. A **74**, 043420 (2006).
[53] T. Dziubak and J. Matulewski, Eur. Phys. J. D **59**, 321 (2010).
[54] R. Loudon, Am. J. Phys. **27**, 649 (1959).
[55] L. Haines and D. H. Roberts, Am. J. Phys. **37**, 1145 (1969).
[56] C. L. Hammer, Am. J. Phys. **56**, 281 (1988).

[57] H. Haug and S. W. Koch, *Quantum Theory of the Optical and Electronic Properties of Semiconductors*, 4th ed. (World Scientific, Singapore, 2004).
[58] C. Fuchs and R. v. Baltz, Phys. Rev. B **63**, 085318 (2001).
[59] S. Bednarek, B. Szafran, T. Chwiej, and J. Adamowski, Phys. Rev. B **68**, 045328 (2003).
[60] F. C. Zhang and S. Das Sarma, Phys. Rev. B **33**, 2903 (1986).
[61] P. Colosimo *et al.*, Nat. Phys. **4**, 386 (2008).
[62] M. V. Frolov, N. L. Manakov, T. S. Sarantseva, M. Yu. Emelin, M. Yu. Ryabikin, and A. F. Starace, Phys. Rev. Lett. **102**, 243901 (2009).
[63] J. Tate, T. Auguste, H. G. Muller, P. Salieres, P. Agostini, and L. F. DiMauro, Phys. Rev. Lett. **98**, 013901 (2007).
[64] K. Schiessl, K. L. Ishikawa, E. Persson, and J. Burgdörfer, Phys. Rev. Lett. **99**, 253903 (2007).
[65] K. L. Ishikawa, K. Schiessl, E. Persson, and J. Burgdörfer, Phys. Rev. A **79**, 033411 (2009).
[66] M. V. Frolov, N. L. Manakov, and A. F. Starace, Phys. Rev. Lett. **100**, 173001 (2008).
[67] A. D. Shiner, C. Trallero-Herrero, N. Kajumba, H.-C. Bandulet, D. Comtois, F. Legare, M. Giguere, J.-C. Kieffer, P. B. Corkum, and D. M. Villeneuve, Phys. Rev. Lett. **103**, 073902 (2009).
[68] B. Shan and Z. Chang, Phys. Rev. A **65**, 011804 (2001).
[69] H. R. Reiss, Phys. Rev. A **63**, 013409 (2000).
[70] K. C. Kulander, K. J. Schafer, and J. L. Krause, in *Atoms in Intense Laser Fields*, edited by M. Gavrila (Academic Press, New York, 1992).
[71] H. G. Muller, Phys. Rev. A **60**, 1341 (1999).
[72] X. M. Tong and C. D. Lin, J. Phys. B **38**, 2593 (2005).
[73] A. Fleischer, Phys. Rev. A **78**, 053413 (2008).
[74] H. G. Muller and F. C. Kooiman, Phys. Rev. Lett. **81**, 1207 (1998).
[75] S. Minemoto, T. Umegaki, Y. Oguchi, T. Morishita, A.-T. Le, S. Watanabe, and H. Sakai, Phys. Rev. A **78**, 061402(R) (2008).
[76] H. J. Wörner, H. Niikura, J. B. Bertrand, P. B. Corkum, and D. M. Villeneuve, Phys. Rev. Lett. **102**, 103901 (2009).
[77] J. Levesque, D. Zeidler, J. P. Marangos, P. B. Corkum, and D. M. Villeneuve, Phys. Rev. Lett. **98**, 183903 (2007).
[78] M. D. Feit, J. A. Fleck Jr., and A. Steiger, J. Comput. Phys. **47**, 412 (1982).
[79] J. L. Krause, K. J. Schafer, and K. C. Kulander, Phys. Rev. A **45**, 4998 (1992).
[80] A. A. Gonoskov and I. A. Gonoskov, e-print arXiv:physics/0607120.
[81] M. Lewenstein, Ph. Balcou, M. Yu. Ivanov, A. L'Huillier, and P. B. Corkum, Phys. Rev. A **49**, 2117 (1994).
[82] L. D. Landau and E. M. Lifshitz, *Quantum Mechanics: Non-Relativistic Theory*, 3rd ed. (Pergamon Press, Oxford, 1977).
[83] M. V. Ivanov, J. Phys. B **34**, 2447 (2001).
[84] T. Brabec, M. Yu. Ivanov, and P. B. Corkum, Phys. Rev. A **54**, R2551 (1996).
[85] L. V. Keldysh, Sov. Phys. JETP **20**, 1307 (1965).
[86] K. Y. Kim, A. J. Taylor, J. H. Glownia, and G. Rodriguez, Nat. Photon. **2**, 605 (2008).
[87] J. Dai, N. Karpowicz, and X.-C. Zhang, Phys. Rev. Lett. **103**, 023001 (2009).
[88] H. Wen and A. M. Lindenberg, Phys. Rev. Lett. **103**, 023902 (2009).